Electroforming of Si NCs/p-Si photovoltaic devices: enhancement of the conversion efficiency through resistive switching

J. L. Frieiro,[1,2] J. López-Vidrier,[2,3] O. Blázquez,[4] J. Ibáñez,[5] D. Yazıcıoğlu,[6] S. Gutsch,[6] M. Zacharias,[6] B. Garrido,[1,2] and S. Hernández[1,2,†]

[1]MIND, Department of Electronics and Biomedical Engineering, Universitat de Barcelona, Martí i Franquès 1, E-08028 Barcelona (Spain).

[2]Institute of Nanoscience and Nanotechnology (IN^{2}UB), Universitat de Barcelona, Av. Joan XXIII S/N, E-08028 Barcelona (Spain).

[3]GECFET, Department of Applied Physics, Universitat de Barcelona, Martí i Franquès 1, E-08028 Barcelona (Spain).

[4]Catalonia Institute for Energy Research (IREC), Jardins de les Dones de Negre 1, 2 pl., E-08930 Sant Adrià del Besòs (Barcelona) (Spain).

[5]Geosciences Barcelona (GEO3BCN), CSIC, Lluís Solé i Sabarís s/n, 08028 Barcelona (Spain).

[6]Laboratory of Nanotechnology, Department of Microsystems Engineering (IMTEK), Albert-Ludwigs-Universität Freiburg, Georges-Köhler-Allee 103, D–79110 Freiburg (Germany).

[†]Corresponding Author: shernandez@ub.edu

Abstract

In this work, the relation between the photovoltaic and resistive switching (RS) properties of metal-oxide-semiconductor devices containing Si nanocrystal (Si NC) superlattices is investigated. A first approximation concludes that the low resistance state achieved by the RS process allows for enhanced photogenerated carrier extraction when compared to the high resistance state and pristine devices. By using different current compliance values during the electroforming process, the low resistance state is further modified, improving its conductivity and the collection probability of photogenerated carriers. Conversion efficiency is enhanced by at least one and up to five orders of magnitude by applying different electroforming processes. In addition to promoting the RS properties in these devices, spectral response measurements demonstrate that Si NCs are partially responsible for the optical absorption, and that their contribution is maintained after electroforming. We thus conclude that the proposed methodology can improve the conversion efficiency of this and other multijunction solar cells or structures that also exhibit RS properties. Through RS, a dense network of conductive filaments is promoted in the insulating region, which reduces the travel distance of photocarriers for their collection.

Key words: silicon nanocrystal multilayers, resistive switching, photovoltaic effect, solar cells

1. Introduction

Silicon nanocrystals (Si NCs) have attracted much attention during the last two decades thanks to their higher radiative-transition rate with respect to bulk Si. Moreover, the electronic quantum confinement within the NCs can be engineered by controlling their size, and thus their band gap energy.[1,2] One of the approaches to achieve control on the NC size is depositing alternated nanometric stoichiometric and non-stoichiometric silicon dioxide multilayers (MLs) and applying afterwards a temperature treatment,[3] exhibiting outstanding structural and optical properties. These properties have been exploited in the particular field of photovoltaics, where the combination of higher bandgap Si NCs and bulk Si in a tandem solar cell structure was addressed, aiming at overcoming the Shockley-Queisser limit for single bandgap materials,[4,5] In this frame, several attempts have been carried out, but with little success owing to the inefficient extraction of carriers generated after photon absorption.[6,7] This low performance is due to the insulating nature of the SiO_2 matrix, which, despite conferring Si NCs an excellent potential barrier that favours quantum confinement, it also makes it difficult for the current to flow through the layers, consequently limiting the electrical conductivity of the system.

To solve the drawback of poor charge extraction, several approaches exist in the literature that address the problem in different ways. On one hand, doping the Si NCs and/or the insulating layers has been a commonly employed strategy in the literature for improving their electrical properties,[8,9] by effectively achieving an intrinsic electric field through the Si NCs/SiO_2 MLs, but at the expense of usually employing processes including toxic reactants and inducing some disorder in both the SiO_2 matrix and the Si NCs, which deteriorates the overall optical properties of the system. On the other hand, it is also possible to directly influence the operation of the MLs-containing devices without affecting their fabrication. In this case, and associated with the limited electrical conductivity of SiO_2 and other dielectric layers, it has been recently observed that atomic rearrangement can be induced by applying a strong enough external electric field.[10–13] In SiO_x layers, this electric field can promote a large diffusion of O^{2-} ions that, in turn, contributes to the formation of nanometre-sized conductive filaments (CFs), or conductive paths, that may even lead to the electrical connection of both electrodes.[14,15] As a result, there is a sudden, but controlled, by means of a current compliance (CC), change in the electrical resistivity that can be tuned under certain bias conditions. Being this rearrangement process reversible, the creation or destruction of those conductive paths modifies the device conductivity, giving rise to either high or low resistance states (HRS and LRS, respectively). This effect can occur many times and is known in the literature as resistive switching (RS). This novel phenomenon allows dielectric materials to act, when embedded in the proper device structure, as resistive random-access memories (RRAMs), by employing the intrinsic material properties to mimic the digital behaviour used in memory storage.

The operation of RS devices is not trivial, and it requires an adequate combination of applied voltage and injected current at different steps of the cycle. In the most common structure for this kind of devices, a metal-insulator-metal (MIM) capacitor, the initial dielectric nature of the oxide active material sandwiched between the two metallic electrodes makes it necessary to perform an electroforming process in order to promote the first CF generation. Simultaneously to the creation of conductive paths, a network of oxygen vacancies is also created, which plays a major role in successive cycles of partial oxidation and reduction of the aforementioned paths. Actually, this network of oxygen vacancies remains within the dielectric layer throughout device operation after electroforming, making it more conductive than in the pristine state but with little or no influence on the macroscopic optical properties due to their small size relative to the device.[16] A schematic representation of such described RS process and the different resistance states is detailed in Fig. 1 for a MIM design, using a metal oxide as insulator layer.

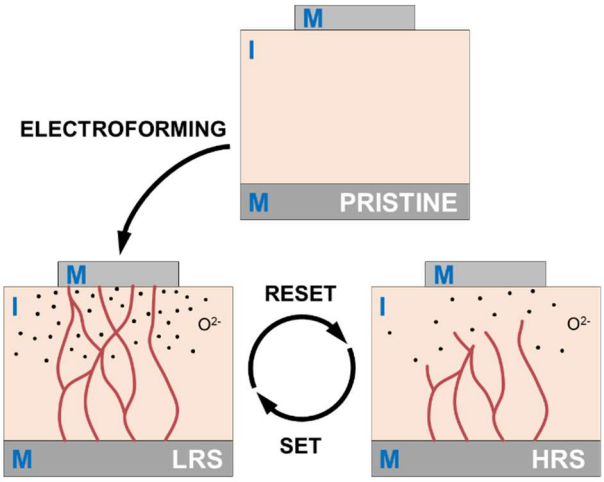

Figure 1. Schematic representation of the complete RS process in a MIM device, with a metal oxide as insulator layer. The insulator is originally in the pristine state. Via an external electric field, the electroforming process is promoted, a network of oxygen ions is liberated from the insulator and CFs are generated, thus achieving the LRS. Under a different electric field polarity, the CFs can be oxidized in the reset process, physically disconnecting the electrodes and reaching the HRS. Similar to electroforming, the set process reconnects the CFs to restore a LRS.

Apart from the purely electric properties exhibited by RS devices, light interaction with these structures has demonstrated to strongly influence on both the writing and the reading of their resistance states. On one hand, RS devices using different semiconductor or dielectric materials (like ZnO or SiO_x) have undergone controlled illumination with the aim of lowering the required voltage for the electroforming process.[17,18] On the other hand, in a previous work employing analogous Si NCs/SiO_2 MLs on a Si substrate, some of the authors observed the possibility to electrically read the resistance state of the devices at $V_{read} = 0$ V, thanks to the photocarriers generated in the substrate and the connections established between the top electrode and the

bottom *p*-type silicon substrate.[13] The combination of the excellent optical properties and their improved electrical conductivity in the LRS after the electroforming in Si NCs can be exploited for photovoltaic (PV) applications, overcoming in this way the high energy barriers that SiO_2 pose to carrier extraction.[19]

In this work we study the light interaction with Si NCs/SiO_2 MLs deposited on a Si substrate after the electroforming process for different CC values ranging from 1 μA to 1 mA. When illuminated with white light at 1000 W m^{-2}, a photocurrent enhancement of more than 5 orders of magnitude with respect to the pristine state has been observed for CC higher than 100 μA. This study demonstrates the possibility of using the RS phenomenon for solving the limited conductivity presented by the top dielectric-embedded Si NCs layers in tandem solar cells.

2. Materials and methods

Devices consisting in 5×Si-rich silicon oxynitride (SRON)/SiO_2 superlattices (SLs), were fabricated by plasma-enhanced chemical-vapour deposition (PECVD) on *p*-type (100)-Si substrates ([B] ~ 10^{16} cm^{-3}, resistivity ~1–20 Ω cm), at a substrate temperature of 375 °C. The thickness of the stoichiometric barrier layer was held constant at 1 nm, found to be optimum for efficient charge transport,[20,21] whereas the thickness of the Si-rich sublayers, with a controlled stoichiometry of $SiO_{0.93}N_{0.23}$ (corresponding to a Si excess of 17 at.%), was nominally fixed at 3.5 nm. Prior to the first SRON sublayer,2-nm-thin Si_3N_4 sublayer was grown on the substrate prior to the first SRON sublayer, with the aim of enhancing electron injection to the MLs in inversion conditions due to the fixed positive charges it contains, consequence of its defective nature.[22,23] A 10-nm capping SiO_2 layer was deposited on top of the structure, thus prevent the samples from further oxidation and keeping the SL structure during the post-deposition annealing process. The SLs were annealed at 1150 °C for 1 hour in a high-purity N_2 atmosphere in order to induce the precipitation and crystallization of the Si excess in the form of Si NCs. The existing dangling bonds were afterwards H_2-passivated. The resulting average NC diameter was found to be d_{NC} = 2.9 nm, as determined by Raman spectroscopy following the same methodology described in Refs. [21,24,25]. After all those processes, the SiO_2 capping layer of 10 nm was removed by wet chemical etching. The final device structure was achieved with a photolithography-patterned 200-nm-thick layer of ZnO deposited by atomic layer deposition on top of the SLs, as transparent conductive oxide (TCO), followed by full-area Al metallization on the bottom of the *p*-type Si substrate, resulting in a final device area of ~7.9×10^{-3} cm^2 (see scheme in the inset of Fig. 2). The overall structure resembles a tandem photovoltaic device, acting the Si substrate as the bottom junction and the Si NCs MLs as the top multijunction, whereas the whole

heterojunction ZnO/Si NC/*p*-Si provide a band offset of about 2 V.[22] Further details on the material and device fabrication processes can be found elsewhere.[20,21,26]

Current-voltage [$I(V)$] characteristics were performed in dark and under illumination by using an Agilent B1500A semiconductor device analyser. The bottom contact (Al) was grounded, whereas voltage was applied on the top contact (ZnO) that was swept from –7 V to 7 V and/or –1 V to 1 V, with slow enough voltage steps to ensure quasi-static conditions (measurements were performed at voltage ramps of 100 mV s^{-1} or 8 mV s^{-1}, respectively). For measurements under illumination, the devices were illuminated with either a white light source (quartz-halogen lamp) or by using a combination of quartz-halogen and Xe lamps coupled to a monochromator with a 2-nm spectral resolution, which allows for monochromatic excitation. The power density of the white illumination is around 1 kW m^{-2}, simulating the optical power of the Sun (solar simulator class B), whereas the power density of monochromatic excitation in the 400–1100 nm spectral range lies in the order of ~0.4–1.2 mW m^{-2}. Electrical current measurements under monochromatic excitation allowed determining the spectral response (SR) of the SL structures. The SR was obtained by measuring the variation, at 0 V, of the current generated under illumination and the residual current existing in dark conditions, and normalized by the incident optical power (i.e., the incident photon flux). The external quantum efficiency (EQE) has been evaluated from the measured SR. Reflectance measurements at normal incidence were carried out with the same monochromator-coupled quartz-halogen and Xe lamps using an integrating sphere.

3. Results and discussion

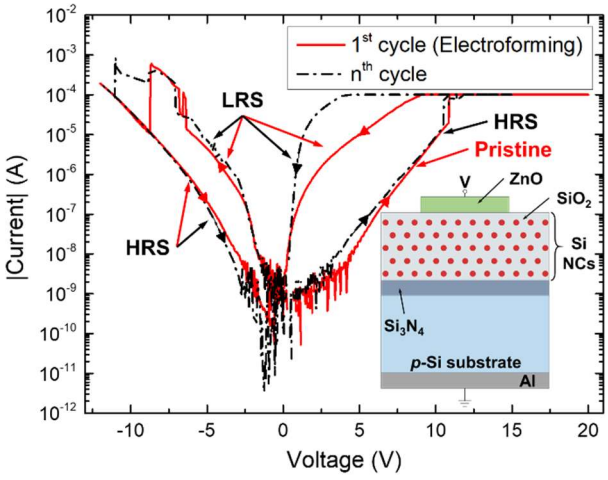

Figure 2. Current-voltage $I(V)$ cycling applied to ZnO/Si NCs/*p*-Si devices resulting in RS. The first cycle displays the electroforming and first reset of the device with a solid red line. A representative (n^{th}) cycle with set and reset processes is depicted with a dashed-dotted black line. Both cycles employ 100 µA as current compliance for the electroforming and set processes. Inset includes a schematic sketch of the device.

In order to obtain the current-voltage $I(V)$ characteristics of the three different resistance states (pristine, LRS and HRS) in dark, the ZnO/Si NCs/*p*-Si devices underwent consecutive $I(V)$ sweeps. Two complete RS cycles are displayed in Fig. 2. Initially, the voltage was increased up to 20 V, using a CC of 100 μA, to induce the electroforming process (solid red curve in Fig. 2). It is evident from the curves that there is a sudden increase in the current at a voltage around 11 V, reaching this CC value. Reducing the voltage down to zero, the change in the $I(V)$ characteristic is clear, as the devices exhibit a much lower resistivity: the device is currently in the LRS. Further reducing the voltage down to –12 V, the current starts increasing (in absolute value) until there is another sudden current decrease at –9 V, indicating an increase in its resistivity: the device lies now in the HRS. Please note that our $I(V)$ curves evidence that the HRS is slightly more conductive than the pristine state, due to the partial formation of the CFs, as it has been reported elsewhere in the literature.[27] After this first voltage sequence, the device underwent subsequent RS cycles alternating from LRS to HRS (a representative one being displayed as the black curve in Fig. 2), as shown in previous works using similar devices.[10]

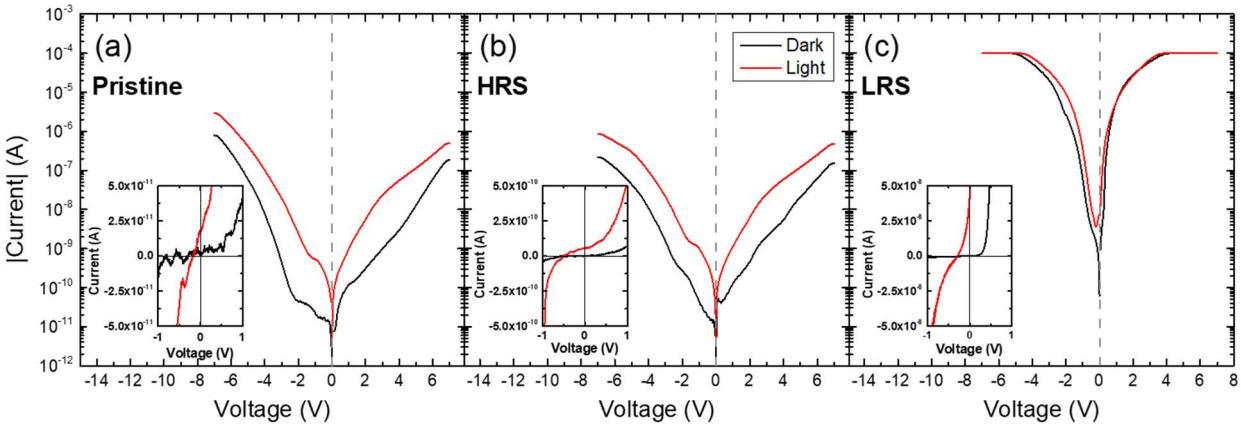

Figure 3. Current-voltage $I(V)$ measurements of the devices under study at the three different RS states: (a) pristine, (b) HRS and (c) LRS, using 100 μA as CC. Black lines correspond to measurements in dark and red lines to measurements under white light illumination. Insets for each state present a zoom-in of the region close to 0 V, allowing the observation of the generated photocurrent.

Using these three different states of the ZnO/Si NCs-SiO_2/*p*-Si devices (pristine, HRS and LRS), we analysed their $I(V)$ characteristics under illumination, comparing them to the ones obtained in dark. In Fig. 3, we present the experimental results obtained for each state in dark and under white light illumination (1 kW m^{-2}). There is a clear current increase at all voltages in pristine and in HRS under illumination (more than one order of magnitude for $V > 2$ V) as a consequence of the photocarriers generated within the whole device structure, thus increasing its conductivity. The situation in the LRS is, however, slightly different since only a rather marginal current increase (a factor 2 at high V) can be observed. As a summary, Table 1 compares the associated resistance values for a commonly employed read voltage of $V_{read} = 0.1$ V, calculated

from the data in Fig 3. As it can be observed, the resistance decreases from pristine to HRS and again in LRS, both in dark and under white light illumination.

Table 1. Associated resistance values for the different states and measurements performed in Fig. 3, at a read voltage of V_{read} = 0.1 V.

	$R_{PRISTINE}$ (MΩ)	R_{HRS} (MΩ)	R_{LRS} (MΩ)
In dark	1.3×10^{4}	2.3×10^{3}	4.6×10^{1}
Under illumination	1.3×10^{3}	1.0×10^{3}	3.3×10^{0}

Apart from the already mentioned increase in the conductivity for all states, all the curves present a sizeable current and voltage either at V = 0 V or I = 0 A, respectively (see insets in Fig. 3), revealing weak but non-negligible short-circuit current (I_{SC}) and open-circuit voltage (V_{OC}) in each state. This is due to the fact that the device structure in the pristine state resembles a *p-i-n* heterojunction, such as the ones devoted to PV applications,[28] which allows extracting some of the photogenerated carriers before their recombination. The inset for each RS state in Fig. 3 displays a zoom-in to the measured voltage range close to 0 V, in linear scale. To obtain reliable results in this range and to avoid either charge trapping or other transient effects (especially for the pristine and HRS states), these measurements were performed under quasi-static conditions, by reducing the voltage ramp down to 8 mV s^{-1}. Indeed, the device in its pristine state already presents a weak short circuit current of about I_{SC} ~ 10 pA (weak, but well above the resolution limit of our experimental set-up, around 0.1 pA) and an open circuit voltage around V_{OC} ~ 160 mV. In the case of the HRS, there are slightly higher values, obtaining I_{SC} ~ 60 pA and V_{OC} ~ 500 mV, which could be related to the increase in its conductivity with respect to the pristine state that facilitates the extraction of the photogenerated carriers. The most impressive results, however, are observed in LRS, where I_{SC} ~ 40 nA, three orders of magnitude higher than in HRS. In addition, we also observed a V_{OC} ~ 280 mV, lower than the one observed in the HRS but much higher than the one in the pristine state.

The observed change in the electrical behaviour, both in dark and under illumination, can be explained by the RS mechanism. With the application of an external electric field, oxygen migration is promoted from the dielectric layer towards the positively-biased electrode, generating a network of oxygen vacancies and conductive filaments of nanometre-sized dimensions that end up connecting top and bottom electrodes.[14] Thus, the presence of higher conductivity sites distributed throughout the dielectric (i.e., the CFs) increases the diffusion length of the photogenerated electron-hole pairs, thus reducing their recombination. This, in turn, facilitates their extraction, which results in the overall improvement of their PV response in terms

of I_{SC} and, to a lesser extent, of V_{OC}. Actually, the density of these CFs distributed along the dielectric layer (i.e., Si NCs/SiO_2) strongly depends on the first electroforming process: an increase in the CC would induce higher oxygen migration, generating a denser network of CFs, that results in an enhanced PV response (although reducing its RS performance).

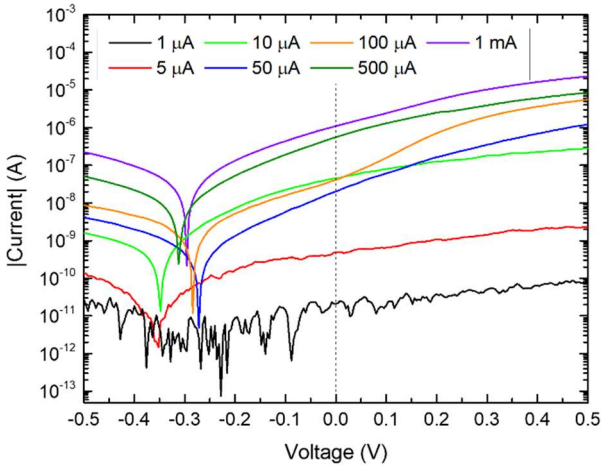

Figure 4. Zoom-in of the quasi-static current-voltage $I(V)$ measurements under white light illumination of the devices under study in LRS after an electroforming process with different CC. The representation of the absolute value in logarithmic scale allows visualizing the I_{SC} as the current at 0 V (dashed line) and the V_{OC} as the voltage at a peak towards low currents (equivalent to the change of sign in linear scale).

To analyse the effect of current compliance on the CF formation and their influence on the PV response, an additional study was performed with a set of different devices initially in the pristine state and submitted to an electroforming process, each of them with a different CC value. After the first CF generation, a $I(V)$ measurement from –1 V to 1 V and under illumination was performed. Figure 4 displays a zoom-in of the –0.5 V to 0.5 V region of the $I(V)$ curves obtained in devices in the LRS where different electrical stress were applied. The $I(V)$ curves show a clear conductivity increase as the limit in the CC during the electroforming process increases, evidencing different LRS. Moreover, all the curves exhibit the same trend observed in Fig. 3c under illumination: there are non-negligible values of I_{SC} and V_{OC}. In Fig. 5a and 5b we have plotted the short-circuit current density (J_{SC}, which is the short-circuit current normalized by the electrode area), and the V_{OC} for each CC value: J_{SC} shows a clear increasing trend, whereas V_{OC} exhibits a mostly constant tendency although with a higher dispersion than the J_{SC}. From these measurements, it can also be extracted the point of maximum output power density ($P_{out,m}$) after the electroforming process, given by

$$P_{\mathrm{out,m}} = J_{\mathrm{m}} \cdot V_{\mathrm{m}} \,, \tag{1}$$

where J_m and V_m correspond to the current density and voltage at the maximum power point, respectively. The values of J_m and V_m have been obtained by numerically evaluating the maximum power extracted. From equation (1), the power efficiency (η) of the devices can be calculated as the ratio between the maximum electrical output power density and the light input power density (P_{in}):

$$\eta = \frac{P_{out,m}}{P_{in}} = \frac{J_m \cdot V_m}{P_{in}}.$$

(2)

In the case of our experimental setup, the light source has an optical power density of P_{in} = 1 kW/m^2. Following equation (2), Fig 5c displays the efficiency corresponding to the devices under test after the aforementioned electroforming processes: the efficiency increases from ~10^{-6} % to 10^{-2} %, when the CC is modified from 1 μA to 1 mA, in good agreement with the observed trend in J_{SC} and V_{OC}.

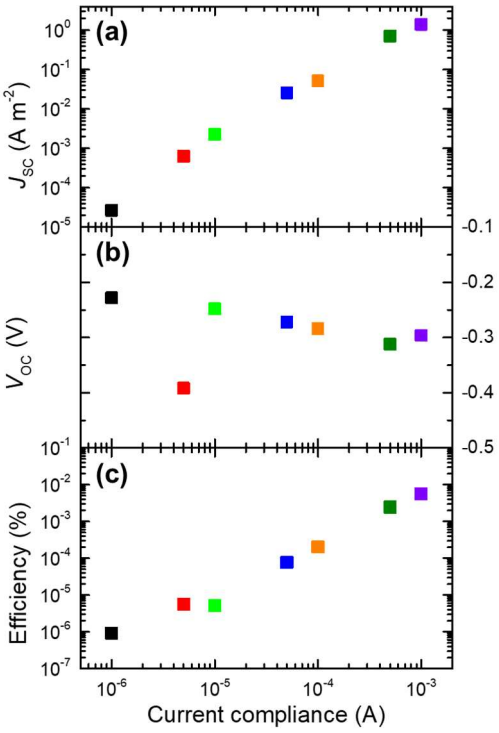

Figure 5. (a) Short-circuit current density, (b) open-circuit voltage and (c) power efficiency in the LRS as a function of the current compliance applied during the electroforming process to a set of initially pristine devices.

The results here presented can relate the trends exhibited by J_{SC}, V_{OC} and the conversion efficiency η to the structural modification taking place in the material. On one hand, for a given incident photon flux, J_{SC} depends on parameters related to geometry (area of the CFs and their number) and photon-to-electron conversion (photon absorption, charge generation and extraction,

diffusion length). Of all these parameters, the carrier diffusion length, and therefore the probability of carriers being collected by the electrodes, can be largely influenced by the generation of a higher number of CFs, whereas the modification of the rest of the parameters has minor (or negligible) contribution, due to the small CF-to-device volume ratio.[16] Indeed, according to the RS filament model, either the size of the filaments or their number increases as CC increases. In this frame, our increasing J_{SC} trend in Fig. 5a can be explained with an increase in the number of filaments –or a combination with an increase of their size– that increases the diffusion length of the insulating layer. In order to be extracted before recombination, photogenerated carriers no longer need to travel the whole thickness of the insulating Si NC/SiO_2 but rather the distance to the closest CF. In contrast, just an increase in the CF size without considering an increase in the number of filaments would not be sufficient to collect so effectively the photogenerated carriers.

On the other hand, Fig. 5b shows not so significant an evolution of V_{OC} with the CC as found for J_{SC}. Indeed, the V_{OC} represents the point where photocarrier generation and recombination are in equilibrium, and it is largely influenced by the reverse saturation current density, J_S, that is, the minority carriers circulating under dark conditions in reverse. Under illumination conditions, the photogenerated carriers recombine with these minority carriers. Since neither the photogeneration nor J_S are expected to be affected by the presence of CFs, the observed small variation of the V_{OC} with a high data dispersion can be mainly attributed to device-to-device variability.

From the results displayed in Fig. 5c, measured in the LRS, it is clear that the PV properties of the Si NCs/SiO_2 MLs are strongly dependent on the extent of the applied electroforming process. In particular, a higher CC increases the extraction efficiency of generated photocarriers by giving rise to a denser network of conductive filaments, through which photocarriers are extracted before their recombination. Focusing on the numerical results, it is found that increasing the current compliance by three orders of magnitude (from 1 μA to 1 mA) results in a conversion efficiency increase of almost four orders of magnitude (from $\eta \sim 10^{-6}$ % to $\eta \sim 10^{-2}$ %). With respect to the pristine state, where extremely low conversion efficiencies of $\eta \sim 10^{-7}$ % are obtained (not shown here), electroforming using the highest CC results in a LRS state with an efficiency gain of almost five orders of magnitude. When reversing towards the HRS, devices exhibit efficiencies of ~10^{-6} %, again demonstrating that the conductivity level of the pristine state is never reached back, owing to the partial re-oxidation of the CFs.

So far, the PV data proved that the structural modification of the dielectric layer (Si NCs/SiO_2 MLs) induced by controlled electroforming improves charge extraction of the devices under study. Nevertheless, this structural rearrangement can also induce alterations in the optical properties of the devices, especially in terms of optical transmission and absorption, which might be of great interest for solar cell applications. In order to analyse the effect of the RS phenomenon

on the optical properties, the EQE of the devices has been determined in the LRS after employing different CC values, from spectral response [$SR(\lambda)$] measurements (current extracted per incident optical power, in A W^{-1}). The *SR* of the devices has been measured in the range of 300–1100 nm and at 0 V, which allows calculating the EQE of the devices by applying the following relation:

$$EQE(\lambda) = SR(\lambda) \cdot \frac{hc}{q\lambda}, \quad (3)$$

where h is the Plank's constant, c is the speed of light in vacuum, q is the elementary charge and λ is the wavelength of the incoming photons. The EQE spectra of the devices submitted to electroforming processes at different CC are displayed in Fig. 6. It is evident that there is an increase of the EQE at all wavelengths as the CC increases, indicating a clear improvement of photocarrier extraction ratio at increasing CC. The results hereby reported again demonstrate that the lower the current limitation (i.e., the higher the CC), the more efficient the carrier extraction and thus quantum efficiency.

From these spectra, the short-circuit current density (J_{SC}) of the devices can be evaluated by considering the solar spectral irradiance $F(\lambda)$ and the experimentally determined reflectance of the devices $R(\lambda)$ and integrating in the range from 300 nm to 1100 nm (limiting the integration range to the near UV, where there is little spectral irradiance, and below bulk-Si band-gap energy, where there is no absorption): [29]

$$J_{SC} = J_L|_{V=0} = \frac{q}{h \cdot c} \cdot \int_{300}^{1100} F(\lambda) \cdot [1 - R(\lambda)] \cdot EQE(\lambda)|_{V=0} \cdot \lambda \cdot d\lambda. \quad (4)$$

For the calculation of J_{SC} with Eq. 4, the $F(\lambda)$ employed corresponded to the AM1.5G standard. When comparing directly measured and calculated from EQE spectra, all values lie within the same order of magnitude and the overall increasing tendency previously observed is maintained. This fact well corroborates that the measurements performed via electrical (current-voltage curves) and electro-optical (spectral response analysis) methods are consistent with each other.

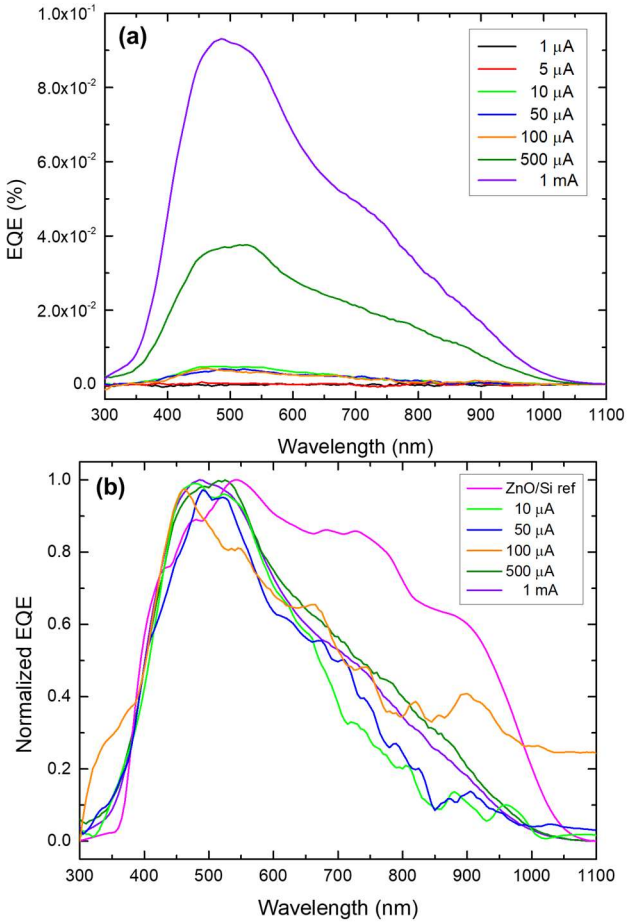

Figure 6. (a) External quantum efficiency spectra in the LRS for each employed current compliance. (b) Normalized EQE for the higher CC and comparison with a ZnO/Si reference device.

Carefully examining the spectra in Fig. 6a, three distinct regions are observed, where the overall intensity is modified in a different way with the CC: (i) lower compliances below 10 μA, which result in almost no modification of the device EQE (as previously stated in Ref. [10], in some cases these limitations result in unstable LRS); (ii) up to 100 μA, where there is an increase in efficiency but differences between different CC values are not significant; and (iii) at large compliances, where increase of efficiency becomes evident (although at this point the resistance state is not reversible, i.e., the device is set to a permanent LRS). Indeed, from this last region it becomes evident that the EQE line-shape is barely modified irrespective of the employed current limitation level.

Comparing the line-shapes of the spectra represented in Fig 6b for different CC, the small differences observable can be identified with device-to-device variability. The spectral line-shape of these devices compared with a reference Si sample has been previously analysed by some of the authors (the reader is kindly redirected to Ref. [13]). It was concluded in that work that whilst the Si substrate is responsible for most of the absorption, Si NCs also contribute, as deduced from a strong signal at short wavelengths and a blueshift at longer wavelengths, both occurrences being

compatible with quantum confinement (and thus the presence of nanostructured Si) within the sample. These features are maintained in the present analysis, as it can be observed by comparison in Fig. 6b with a normalized EQE of the reference device, indicating that even with large CC, CF generation does not induce a lateral percolation of the Si NC networks,[30,31] and therefore confinement of the Si NCs is still maintained. It is therefore possible to conclude that, under the current limitations employed in this study, the induced rearrangement of randomly-distributed oxygen vacancies through the dielectric layer results in an increase of the overall electrical conductivity and thus carrier extraction, while barely affecting the optical absorption of the presented devices.

Some authors have previously reported the effect of ferroelectric resistive switching in the photovoltaic properties of ferroelectric materials, where the change in resistance modifies their conduction and the interface with the electrodes.[32–35] These works are mainly focused on the possibility of optically reading the device state, without exploring the possible advantages of RS in tandem PV systems. The presented methodology, namely the utilization of controlled RS on PV absorber materials to improve CF generation, is validated by our results and has shown an improvement in solar cell efficiency. This can be extended to other high-bandgap absorbing materials which simultaneously exhibit RS phenomenon, to further enhance their extraction efficiency.

4. Conclusions

In this work, the RS methodology has been employed in combination with electro-optical measurements in ZnO/(SiNCs/SiO_2 MLs)/*p*-Si photovoltaic devices. A great enhancement of the PV conversion efficiency of such devices has been achieved after electroforming, inducing controlled nanoscale modifications within the dielectric layer in the form of oxygen vacancies rearrangement and the consequent formation of CFs. In particular, compared to the pristine and HRS states, when the devices lay in the LRS they allow a more efficient photogenerated-carriers extraction under either high-power white-light (class B solar simulator) or low-power monochromatic-light illumination. In addition, the use of higher CC values to limit the LRS is translated into enhanced carrier extraction by increasing the density of the CF network, thus attaining a higher collection probability. Finally, the spectral analysis of photon-to-electron conversion in LRS and its comparison with a reference Si device has identified the non-negligible absorption of Si NCs within the system, which is maintained at larger current compliances indicating a small scale of structural modifications that do not completely eliminate the quantum confinement properties associated to Si nanostructures. Overall, the presented RS procedure

applied to multijunction photovoltaic devices greatly improves their carrier extraction efficiency while maintaining the optical properties, resulting in an enhancement in their PV performance.

Acknowledgements

This work was financially supported by the Spanish Ministry of Economy, Industry and Competitiveness (TEC2016-76849-C2-1-R) and the German Research Foundation (ZA191/27-3 and ZA191/33-1). J.L.F. acknowledges financial support from the subprogram "Ayudas para la Formación de Profesorado Universitario" (FPU16/06257) from the Spanish Ministry of Education, Culture and Sports.

References

[1] F. Iacona, G. Franzò, C. Spinella, Correlation between luminescence and structural properties of Si nanocrystals, J. Appl. Phys. 87 (2000) 1295–1303. https://doi.org/10.1063/1.372013.

[2] T. van Buuren, L.N. Dinh, L.L. Chase, W.J. Siekhaus, L.J. Terminello, Changes in the Electronic Properties of Si Nanocrystals as a Function of Particle Size, Phys. Rev. Lett. 80 (1998) 3803–3806. https://doi.org/10.1103/PhysRevLett.80.3803.

[3] M. Zacharias, J. Heitmann, R. Scholz, U. Kahler, M. Schmidt, J. Bläsing, Size-controlled highly luminescent silicon nanocrystals: A SiO/SiO 2 superlattice approach, Appl. Phys. Lett. 80 (2002) 661–663. https://doi.org/10.1063/1.1433906.

[4] P. Würfel, Physics of Solar Cells, Wiley, 2005. https://doi.org/10.1002/9783527618545.

[5] M.A. Green, Third generation photovoltaics: solar cells for 2020 and beyond, Phys. E Low-Dimensional Syst. Nanostructures. 14 (2002) 65–70. https://doi.org/10.1016/S1386-9477(02)00361-2.

[6] I. Perez-Wurfl, L. Ma, D. Lin, X. Hao, M.A. Green, G. Conibeer, Silicon nanocrystals in an oxide matrix for thin film solar cells with 492mV open circuit voltage, Sol. Energy Mater. Sol. Cells. 100 (2012) 65–68. https://doi.org/10.1016/j.solmat.2011.02.029.

[7] L. Wu, T. Zhang, Z. Lin, X. Jia, B. Puthen-Veettil, T. Chien-Jen Yang, H. Xia, G. Conibeer, I. Perez-Wurfl, Silicon nanocrystal photovoltaic device fabricated via photolithography and its current–voltage temperature dependence, Sol. Energy Mater. Sol. Cells. 128 (2014) 435–440. https://doi.org/10.1016/j.solmat.2014.06.007.

[8] D. Hiller, J. López-Vidrier, S. Gutsch, M. Zacharias, K. Nomoto, D. König, Defect-Induced Luminescence Quenching vs. Charge Carrier Generation of Phosphorus

Incorporated in Silicon Nanocrystals as Function of Size, Sci. Rep. 7 (2017) 863. https://doi.org/10.1038/s41598-017-01001-1.

[9] D. Hiller, J. López-Vidrier, S. Gutsch, M. Zacharias, M. Wahl, W. Bock, A. Brodyanski, M. Kopnarski, K. Nomoto, J. Valenta, D. König, Boron-Incorporating Silicon Nanocrystals Embedded in SiO2: Absence of Free Carriers vs. B-Induced Defects, Sci. Rep. 7 (2017) 8337. https://doi.org/10.1038/s41598-017-08814-0.

[10] J.L. Frieiro, J. López-Vidrier, O. Blázquez, D. Yazlcloğlu, S. Gutsch, J. Valenta, S. Hernández, M. Zacharias, B. Garrido, Silicon nanocrystals-based electroluminescent resistive switching device, J. Appl. Phys. 126 (2019) 144501. https://doi.org/10.1063/1.5119299.

[11] K.E. González–Flores, B. Palacios-Márquez, J. Álvarez–Quintana, S.A. Pérez–García, L. Licea–Jiménez, P. Horley, A. Morales-Sánchez, Resistive switching control for conductive Si-nanocrystals embedded in Si/SiO 2 multilayers, Nanotechnology. 29 (2018) 395203. https://doi.org/10.1088/1361-6528/aad24d.

[12] K.E. González-Flores, P. Horley, S.A. Cabañas-Tay, S.A. Pérez-García, L. Licea-Jiménez, L. Palacios-Huerta, M. Aceves-Mijares, M. Moreno-Moreno, A. Morales-Sánchez, Analysis of the conduction mechanisms responsible for multilevel bipolar resistive switching of SiO2/Si multilayer structures, Superlattices Microstruct. 137 (2020). https://doi.org/10.1016/j.spmi.2019.106347.

[13] J. López-Vidrier, J.L. Frieiro, O. Blázquez, D. Yazicioglu, S. Gutsch, K.E. González-Flores, M. Zacharias, S. Hernández, B. Garrido, Photoelectrical reading in ZnO/Si NCs/ p -Si resistive switching devices, Appl. Phys. Lett. 116 (2020) 193503. https://doi.org/10.1063/5.0005069.

[14] A. Mehonic, S. Cueff, M. Wojdak, S. Hudziak, O. Jambois, C. Labbé, B. Garrido, R. Rizk, A.J. Kenyon, Resistive switching in silicon suboxide films, J. Appl. Phys. 111 (2012) 074507. https://doi.org/10.1063/1.3701581.

[15] A. Mehonic, M.S. Munde, W.H. Ng, M. Buckwell, L. Montesi, M. Bosman, A.L. Shluger, A.J. Kenyon, Intrinsic resistance switching in amorphous silicon oxide for high performance SiO x ReRAM devices, Microelectron. Eng. 178 (2017) 98–103. https://doi.org/10.1016/j.mee.2017.04.033.

[16] O. Blázquez, J.L. Frieiro, J. López-Vidrier, C. Guillaume, X. Portier, C. Labbé, P. Sanchis, S. Hernández, B. Garrido, Resistive switching and charge transport mechanisms in ITO/ZnO/ p -Si devices, Appl. Phys. Lett. 113 (2018) 183502. https://doi.org/10.1063/1.5046911.

[17] O. Blázquez, J.L. Frieiro, J. López-Vidrier, C. Guillaume, X. Portier, C. Labbé, S. Hernández, B. Garrido, Light-activated electroforming in ITO/ZnO/ p -Si resistive switching devices, Appl. Phys. Lett. 115 (2019). https://doi.org/10.1063/1.5125844.

[18] A. Mehonic, T. Gerard, A.J. Kenyon, Light-activated resistance switching in SiOx RRAM devices, Appl. Phys. Lett. 111 (2017) 1200. https://doi.org/10.1063/1.5009069.

[19] G. Conibeer, M. Green, R. Corkish, Y. Cho, E.-C. Cho, C.-W. Jiang, T. Fangsuwannarak, E. Pink, Y. Huang, T. Puzzer, T. Trupke, B. Richards, A. Shalav, K. Lin, Silicon nanostructures for third generation photovoltaic solar cells, Thin Solid Films. 511–512 (2006) 654–662. https://doi.org/10.1016/j.tsf.2005.12.119.

[20] S. Gutsch, J. Laube, A.M. Hartel, D. Hiller, N. Zakharov, P. Werner, M. Zacharias, Charge transport in Si nanocrystal/SiO 2 superlattices, J. Appl. Phys. 113 (2013) 133703. https://doi.org/10.1063/1.4798395.

[21] J. López-Vidrier, Y. Berencén, S. Hernández, B. Mundet, S. Gutsch, J. Laube, D. Hiller, P. Löper, M. Schnabel, S. Janz, M. Zacharias, B. Garrido, Structural parameters effect on the electrical and electroluminescence properties of silicon nanocrystals/SiO 2 superlattices, Nanotechnology. 26 (2015) 185704. https://doi.org/10.1088/0957-4484/26/18/185704.

[22] J. López-Vidrier, S. Gutsch, O. Blázquez, J. Valenta, D. Hiller, J. Laube, J. Blanco-Portals, L. López-Conesa, S. Estradé, F. Peiró, B. Garrido, S. Hernández, M. Zacharias, Effect of Si3N4-Mediated Inversion Layer on the Electroluminescence Properties of Silicon Nanocrystal Superlattices, Adv. Electron. Mater. 4 (2018) 1700666. https://doi.org/10.1002/aelm.201700666.

[23] Y. Berencén, J.M. Ramírez, O. Jambois, C. Domínguez, J.A. Rodríguez, B. Garrido, Correlation between charge transport and electroluminescence properties of Si-rich oxide/nitride/oxide-based light emitting capacitors, J. Appl. Phys. 112 (2012) 033114. https://doi.org/10.1063/1.4742054.

[24] J. López-Vidrier, S. Hernández, D. Hiller, S. Gutsch, L. López-Conesa, S. Estradé, F. Peiró, M. Zacharias, B. Garrido, Annealing temperature and barrier thickness effect on the structural and optical properties of silicon nanocrystals/SiO 2 superlattices, J. Appl. Phys. 116 (2014) 133505. https://doi.org/10.1063/1.4896878.

[25] S. Hernández, J. López-Vidrier, L. López-Conesa, D. Hiller, S. Gutsch, J. Ibáñez, S. Estradé, F. Peiró, M. Zacharias, B. Garrido, Determining the crystalline degree of silicon nanoclusters/SiO2 multilayers by Raman scattering, J. Appl. Phys. 115 (2014). https://doi.org/10.1063/1.4878175.

[26] A.M. Hartel, D. Hiller, S. Gutsch, P. Löper, S. Estradé, F. Peiró, B. Garrido, M. Zacharias, Formation of size-controlled silicon nanocrystals in plasma enhanced chemical vapor deposition grown SiOxNy/SiO2 superlattices, Thin Solid Films. 520 (2011) 121–125. https://doi.org/10.1016/j.tsf.2011.06.084.

[27] R. Waser, R. Dittmann, C. Staikov, K. Szot, Redox-based resistive switching memories nanoionic mechanisms, prospects, and challenges, Adv. Mater. 21 (2009) 2632–2663. https://doi.org/10.1002/adma.200900375.

[28] J. Valenta, S. Mirabella, Nanotechnology and Photovoltaic Devices, Jenny Stanford Publishing, 2015. https://doi.org/10.1201/b18090.

[29] S.M. Sze, K.K. Ng, Physics of Semiconductor Devices, John Wiley & Sons, Inc., Hoboken, NJ, USA, 2006. https://doi.org/10.1002/0470068329.

[30] S. Gutsch, D. Hiller, J. Laube, M. Zacharias, C. Kübel, Observing the morphology of single-layered embedded silicon nanocrystals by using temperature-stable TEM membranes, Beilstein J. Nanotechnol. 6 (2015) 964–970. https://doi.org/10.3762/bjnano.6.99.

[31] J. Laube, S. Gutsch, D. Wang, C. Kübel, M. Zacharias, D. Hiller, Two-dimensional percolation threshold in confined Si nanoparticle networks, Appl. Phys. Lett. 108 (2016) 043106. https://doi.org/10.1063/1.4940971.

[32] L. Zhang, J. Chen, J. Cao, D. He, X. Xing, Large resistive switching and switchable photovoltaic response in ferroelectric doped BiFeO3-based thin films by chemical solution deposition, J. Mater. Chem. C. 3 (2015) 4706–4712. https://doi.org/10.1039/c5tc00814j.

[33] H. Fan, C. Chen, Z. Fan, L. Zhang, Z. Tan, P. Li, Z. Huang, J. Yao, G. Tian, Q. Luo, Z. Li, X. Song, D. Chen, M. Zeng, J. Gao, X. Lu, Y. Zhao, X. Gao, J.M. Liu, Resistive switching and photovoltaic effects in ferroelectric BaTiO3-based capacitors with Ti and Pt top electrodes, Appl. Phys. Lett. 111 (2017) 252901. https://doi.org/10.1063/1.4999982.

[34] B. Xu, G. Wang, Y. Zhou, Q. Li, Q. Xu, Improving the photovoltaic effect by resistive switching, Appl. Phys. Lett. 113 (2018) 133901. https://doi.org/10.1063/1.5039590.

[35] L. Huang, M. Wei, C. Gui, L. Jia, Ferroelectric photovoltaic effect and resistive switching behavior modulated by ferroelectric/electrode interface coupling, J. Mater. Sci. Mater. Electron. 31 (2020) 20667–20687. https://doi.org/10.1007/s10854-020-04600-3.